



OPEN

SUBJECT AREAS:

NANOPARTICLES
CATALYTIC MECHANISMS
STRUCTURAL PROPERTIES
METALS AND ALLOYSReceived
27 June 2013Accepted
1 November 2013Published
14 January 2014Correspondence and
requests for materials
should be addressed to
C.-M.W. (chongmin.
wang@pnnl.gov)

In-Situ TEM visualization of vacancy injection and chemical partition during oxidation of Ni-Cr nanoparticles

Chong-Min Wang¹, Arda Genc², Huikai Cheng², Lee Pullan², Donald R. Baer¹ & Stephen M. Brummer³¹Environmental Molecular Sciences Laboratory, Pacific Northwest National Laboratory, Richland, WA 99352, USA, ²FEI Company, 5350 NE Dawson Creek Drive, Hillsboro, Oregon 97124, USA, ³Fundamental and Computational Science Directorate, Pacific Northwest National Laboratory, Richland, WA 99352, USA.

Oxidation of alloy often involves chemical partition and injection of vacancies. Chemical partition is the consequence of selective oxidation, while injection of vacancies is associated with the differences of diffusivity of cations and anions. It is far from clear as how the injected vacancies behave during oxidation of metal. Using in-situ transmission electron microscopy, we captured unprecedented details on the collective behavior of injected vacancies during oxidation of metal, featuring an initial multi-site oxide nucleation, vacancy supersaturation, nucleation of a single cavity, sinking of vacancies into the cavity and accelerated oxidation of the particle. High sensitive energy dispersive x-ray spectroscopy mapping reveals that Cr is preferentially oxidized even at the initial oxidation, leading to a structure that Cr oxide is sandwiched near the inner wall of the hollow particle. The work provides a general guidance on tailoring of nanostructured materials involving multi-ion exchange such as core-shell structured composite nanoparticles.

Oxidation of metallic materials in either pure element or alloy form is familiar to all of us with significant technological, environmental, safety and economic impact^{1–3}. Microscopically, oxidation involves the reaction of oxygen with the very surface layer of metallic element to form a thin layer of oxide⁴. Upon the initial formation of oxidation layer on the metal surface, the subsequent oxidation progresses by a combination of inward diffusion of oxygen and outward diffusion of metal ion through the oxide layer^{5–7}. The rate of oxidation and the consequences of the microstructure of the oxidized product depend on the relative diffusivity of oxygen and metallic ions through the growing oxide film. If the diffusivity of metallic ion in the oxide layer is larger than oxygen, it would lead to the injection of vacancies into the system and consequently condensation of the vacancies will lead to the formation of a cavity within the structure. Differences on the diffusivity of cation and anion across the oxide layer (Kirkendall effect)⁸ has been smartly used to, at nanoscale, tailor nanoparticles of unique topographical structure and spatial chemical characteristics, typically including hollow^{9–13}, core-shell¹⁴, and compositionally graded nanoparticles^{15,16}. As compared with the pure element, the oxidation behavior of metallic alloy is further influenced by the presence of multiple cations having different oxidation energies and rates of diffusion, such as possibly involving selective oxidation of one component of the alloy. A selective oxidation, in essence, can be disadvantage or advantage. Typically, oxidation resistance of superalloy is relied on preferential oxidation of Cr to form a Cr₂O₃ layer, which prevents the oxidation of the underlying Ni^{3,17}.

It has been generally realized that the oxidation of metal and the corresponding structural and chemical evolution of the whole system is determined by the dynamic interaction of diffusing species and defects (such as vacancies). Recent work, for example, suggests that vacancy injection during oxidation of material at a crack tip may enhance stress corrosion cracking¹⁸. Direct atomic level observation of interaction of diffusing species with defects and defect clusters has not been established. We are particularly interested in understanding the impact of alloy composition on vacancy injection. Measurements on nanoparticles provide a method of observing the process in some detail. In this paper we report the direct dynamic observation of structural evolution of pure Ni and Ni doped with 5 at% Cr upon oxidation. The oxidation experiment was carried out using aberration corrected environmental TEM (ETEM), which allows establishing of up to 20 mbar pressure around the sample while in imaging mode. These in-situ TEM oxidation experiments provide us the opportunity for direct visualization of the dynamics structural evolution of the nanoparticle during high temperature oxidation^{19,20}. In combination with sensitive energy dispersive x-ray analysis (EDS) and high spatial scanning TEM (STEM) electron energy loss



spectroscopy (EELS) analysis, we have gained unprecedented information regarding the chemistry and vacancy injection characteristics during the oxidation process of Ni and Ni doped with 5 at% Cr.

Results

Oxidation behavior and microstructure of oxidized particle. The detailed microstructural feature of the as-prepared Ni and Ni5Cr nanoparticles has been analyzed using a combination of XRD, electron diffraction, HRTEM imaging, XPS, and EELS, with the results reported previously²¹. In this work, we focus on the high temperature oxidation and the corresponding structural and chemical evolution during the oxidation. The oxidation experiment was uniquely designed such that we can monitor the microstructural evolution of a specific particle with the progress of the oxidation. Figure 1 shows the structural evolution of the particle oxidized at 200 °C in air. For both Ni and Ni5Cr particles, the oxidation at 200 °C in air progresses in a core-shell fashion, with the thickness of the oxide layer increase gradually with the oxidation time and this is illustrated in the TEM images of Figure 1 (a) through (d). The oxide shell thickness as a function oxidation time was drawn in Figure 1 (e) for Ni and Ni5Cr particle. The oxide layer thickness as a function of oxidation time at 200 °C in air follows a parabolic behavior. As evidenced from Figure 1(e), it can be noticed that following the same time of oxidation, the shell thickness on the

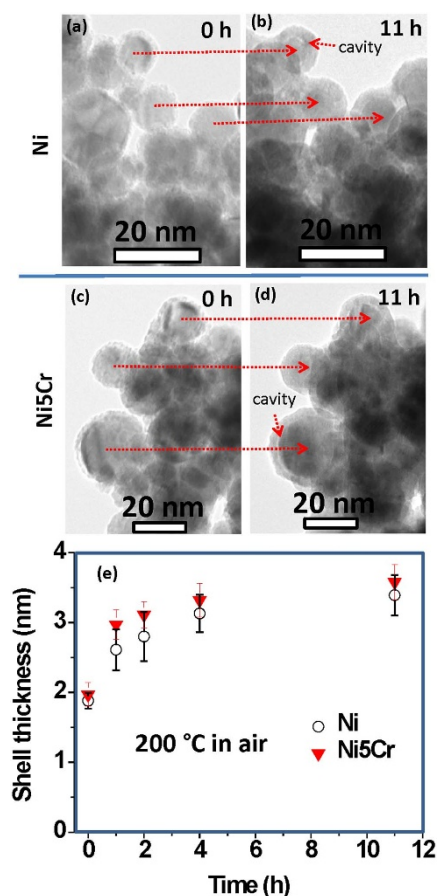


Figure 1 | Microstructural feature and oxidation kinetics of Ni particles oxidized at 200 °C in air. (a) Ni particles before oxidation; (b) the particles shown in (a) were oxidized for 11 hours. (c) Ni5Cr particles before oxidation; (d) the particles shown in (c) were oxidized for 11 hours. (e) The oxide shell thickness as a function of oxidation time, revealing a parabolic oxidation behavior. Note the small cavities trapped at the interface between the metal and oxide layer as arrowed.

particle doped with Cr is slightly thicker than that of pure Ni. This observation likely indicates that with the doping of Cr into Ni, the oxidation rate increases. Carefully checking of the interface between the oxide layer and the metal core, we noticed that there are small cavities at the interface as indicated in Fig. 1(b) and (d). Formation of cavity is the consequence of the vacancy injection due to the diffusion of cation is faster than oxygen as described in detail in a previous publication¹⁰.

The vacancy injection is further manifested by the oxidation of the particle at 300 °C in air as illustrated in Figure 2. We noticed that following 1 hour oxidation in air at 300 °C, the particles of both Ni and Ni5Cr are fully oxidized. The microstructure of the fully oxidized particle is featured by a cavity formation within the polycrystalline oxide shell (Figure 2 (a) through (f)). As defined in the schematic drawing of the Figure 2 (a) and (b), the size of the cavity as compared with the initial particle size is a measure of vacancies injected during the oxidation of the particle. The parameter R, defined as $R = d_3/d_2$,

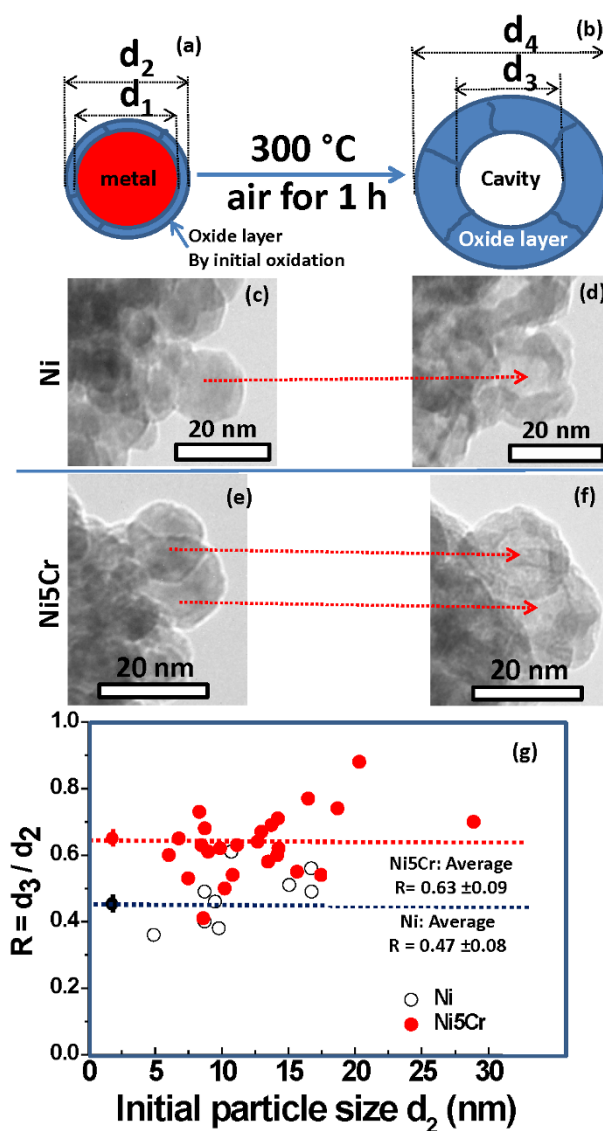


Figure 2 | Microstructural feature of Ni particles oxidized at 300 °C in air for 1 hour. (a) and (b) Schematic drawings showing oxidation leads to a hollow structured particle. (c) Ni particles before oxidation; (d) the particles shown in (c) were oxidized for 1 hour. (e) Ni5Cr particles before oxidation; (f) the particles shown in (e) were oxidized for 1 hour. (g) Dependence of R parameter on the initial particle size for Ni and Ni5Cr particles.



is a quantitative evaluation of the relative diffusivity of cation and oxygen during the oxidation. The larger of the R value, the larger of the difference in the diffusivity between cation and oxygen. For the two extreme situations, if $R = 1$, this means that during the oxidation, the cation only diffuses out without oxygen diffusion (mean a high generation of vacancies). If $R = 0$, then the oxygen diffusivity equals to the diffusivity of cation (lower amount of vacancy formation). The R value for both Ni and Ni5Cr particle is statistically measured on the sample oxidized at 300°C in air and is plotted in Figure 2(g) as a function of initial particle size. Figure 2(g) indicates that the R value shows no significant dependence on the initial particle size. For Ni particle, the R values is scattered around an average value of 0.47 ± 0.08 , while for Ni5Cr particle, R has an average value of 0.63 ± 0.09 . For both Ni and Ni5Cr, the R is less than 1, indicating that during the oxidation, the cation is apparently diffusing faster than oxygen. The R value for Ni5Cr is larger than that of Ni, suggesting that following the doping of 5% Cr in Ni, the cation diffusivity is increased, which consequently leads to the increasing of vacancy injection rate. This appears to be consistent with the result of the oxide layer thickness as a function of oxidation time shown in Figure 1(e) for which the oxidation rate of Ni5Cr is slightly higher than that of Ni.

Direct in-situ TEM observation of structural evolution during high temperature oxidation. The detailed structural evolution of the nanoparticle during the high temperature oxidation is revealed by direct in-situ TEM observation. This is illustrated by the movies shown in the Supporting Information (Movie-S1, Movie-S2, and Movie-S3). As a representative case, Figure 3 shows the captured video frames of structural evolution of a single particle with respect to the progression of the oxidation. As shown in Figure 3 (b) and (c) and the Movie-S1 in the Supporting Materials, we noticed that during the oxidation, the interface between the metal and oxide becomes faceted. At the faceted interface, there are atomic ledges and the oxidation happens through the sweeping of atomic ledges along the interface. Similar oxidation mechanism has been also observed for the case of oxidation of Cu²². The oxidation was initiated by multi-site nucleation of oxides on the metal nanoparticle surface

(Figure 3(c)). Growth of the oxide nanoparticles on the metal nanoparticles surface leads to the impingement of the oxides, which yields the formation of an oxide layer and generation of grain boundaries within the oxide layer (Figure 3(d)). Upon the formation of the oxide layer, the injected vacancies cannot effectively escape to the surface of the particle, which may lead to the supersaturation of the vacancies during the continued oxidation of the particle. Most dramatically, we found that the clustering of the injected vacancies during the oxidation leads to the nucleation of cavity as illustrated in Figure 3(e)). As soon as the cavity forms, it becomes an effective sink for the vacancies injected with subsequently continued oxidation, therefore, leading to the growth of the cavity. Although it is very hard to quantify the oxidation rate during the in-situ experiment due to the impingement of the oxide particle, we noticed that upon the nucleation of the cavity, the oxidation appears to be accelerated. This feature is well supported by the videos in the Supporting Information (Movie-S1, S2, S3).

Chemical partition associated with selective oxidation of Cr in the Ni5Cr alloy. One of the key questions for the oxidation of bi-metallic alloy is if the oxidation happens homogeneously for all the components or one element is preferentially oxidized than the other. To explore if there is any selective oxidation for the case of Ni5Cr alloy, we use high sensitive EDS in a STEM to map the spatial distribution of Cr, O, and Ni in the particle before and after high temperature oxidation. As representatively illustrated in Figure 4, the EDS mapping reveals that the thin oxide layer formed during the air exposure of the particle at room temperature (which is normally termed as initial oxidation) is enriched with Cr and O. This observation is further supported by the additional EDS maps in the Supporting Information (Figure S1). The high concentration of O at the surface of the particle is not a surprise. Based on XPS analysis of Ni and Ni5Cr particle, we have found that the particle surface is actually covered by hydroxyls as reported in a prior publication²¹. The enrichment of Cr in the oxide layer formed during the initial oxidation indicates that the Cr is preferentially oxidized even at room temperature. Given the particle size is in the range of ~ 20 nm, selective oxidation of Cr in the Ni5Cr nanoparticle suggests that

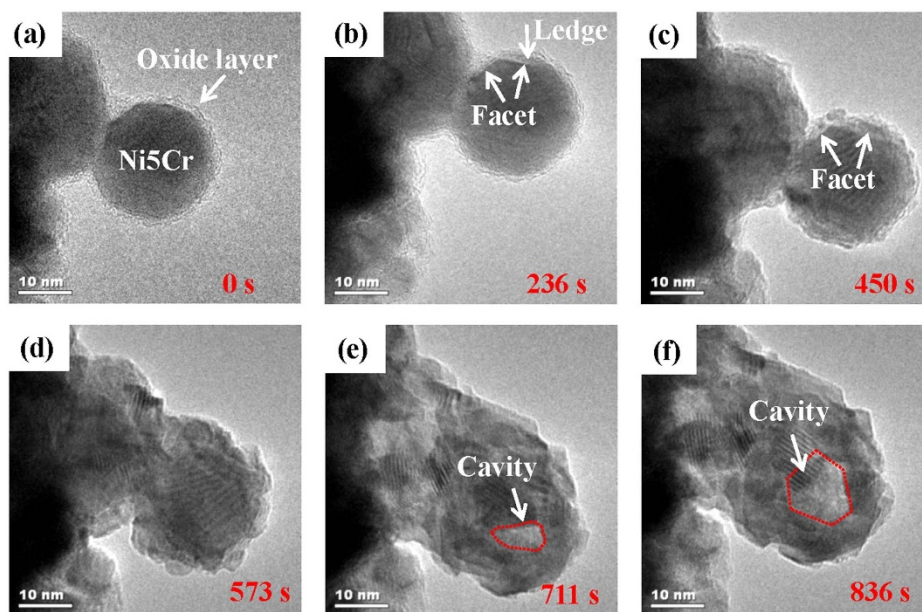


Figure 3 | Captured video frames of time series to illustrate the structural evolution of a single Ni5Cr particle during in-situ TEM oxidation at 375°C with 1 mbar of gas mixture of 25% O₂ and 75% Ar. (a) 0 s; (b) 236 s, note the faceting of the interface between the oxide and metal core as well as the ledge formation at the facet. (c) 450 s, note the multi-site nucleation of oxide and sweeping of the ledge at the faceted interface. (d) 573 s, growth and impingement of the oxide leads to the formation a thick oxide layer. (e) Supersaturation of vacancies lead to the nucleation of a single cavity. (f) Sinking of the injected vacancies leads to accelerated oxidation. These features were vividly revealed in the Movie-S1 in the supporting information.



the Cr is rather mobile in the lattice of Ni even at room temperature within a scale of ~ 10 nm (half of the particle size).

The Cr-rich layer formed during the initial oxidation can serve as a mark for monitoring the high temperature oxidation behavior of the particle. During the high temperature oxidation of the Ni5Cr particle, the Ni will diffuse out and O diffuse inward through this Cr-rich layer. Therefore, for the fully oxidized particle, the spatial location of the Cr-rich layer relative to the cavity within the particle is related to the relative diffusivity of O and Ni in the Cr-rich layer. If the O diffusivity can be neglected as compared with that of Ni, the Cr-rich layer should be just located at the inner wall of the cavity. STEM HAADF image and EDS maps shown in Figure 5 give a complete picture regarding the spatial correlation of the Cr-rich layer and the cavity. From Figure 5 and the additional EDS maps shown in the Supporting Information (Figure S2), we can generally conclude that the diameter of the Cr-rich layer is larger than the cavity. Therefore, the Cr-rich layer is actually sandwiched within the nickel oxide layer. This structural feature is illustrated by the schematic drawing in Figure 5(h). Formation of Cr-rich oxide layer on the surface of the particle will promote the diffusivity of cation as compare with that of NiO. This explains the fact that the cavity in the Ni5Cr is larger than that in Ni as shown in Figure 2(g).

Discussion

Our in-situ TEM observation and EDS mapping clearly indicates that room temperature exposure of ~ 5 at% Cr-doped Ni nanoparticle in air leads to the preferential oxidation of Cr. The nature of the oxidized Cr is not known, such as if it is Cr_2O_3 or it is a complex of

oxides of Cr and Ni. Identification of the true structural nature of the Cr oxide is further complicated by the fact that it is embedded into the NiO matrix following the complete oxidation of the nanoparticle. STEM-EELS mapping indeed indicates that the Cr rich oxide is spatially distributed as particle of ~ 1 nm. Overall, the observation of preferential oxidation of Cr at dilute concentration is consistent with the case of high temperature oxidation of Ni-Cr superalloy for which the Cr is preferentially oxidized to form Cr_2O_3 , subsequently preventing further oxidation of Ni^{3,23}. However, this type of superalloy normally contains about ~ 20 at% Cr, which is far more than what has been incorporated in the nanoparticle in the present work. Furthermore, it is known that for the high temperature oxidation of Ni-Cr, the oxidation rate shows dependence on the Cr concentration. Andreev *et al.*²⁴ reported that for Ni-Cr alloy with 10 at% Cr, the high temperature oxidation rate of the alloy is increased due to the high self-diffusivity of NiO lattice. Collecting all these together, the structural and chemical evolution during the high temperature oxidation of the Ni5Cr particle can be generally schematically shown in Figure 6, featuring enrichment of Cr in the oxide layer during the initial oxidation, subsequent multi-site oxide nucleation and growth when oxidized at high temperature, vacancy supersaturation and nucleation of cavity, fast sinking of vacancies into the cavity and accelerated oxidation. It should be pointed out that it is well established that there is a “critical” concentration of protective elements (e.g. Cr) to form a slowly diffusion layer^{3,17}. When below that threshold the layers that form or try to form are not protective. We would not expect the 5% Cr alloy to form a protective layer. We are interested in understanding how alloy composition alters the ratio of

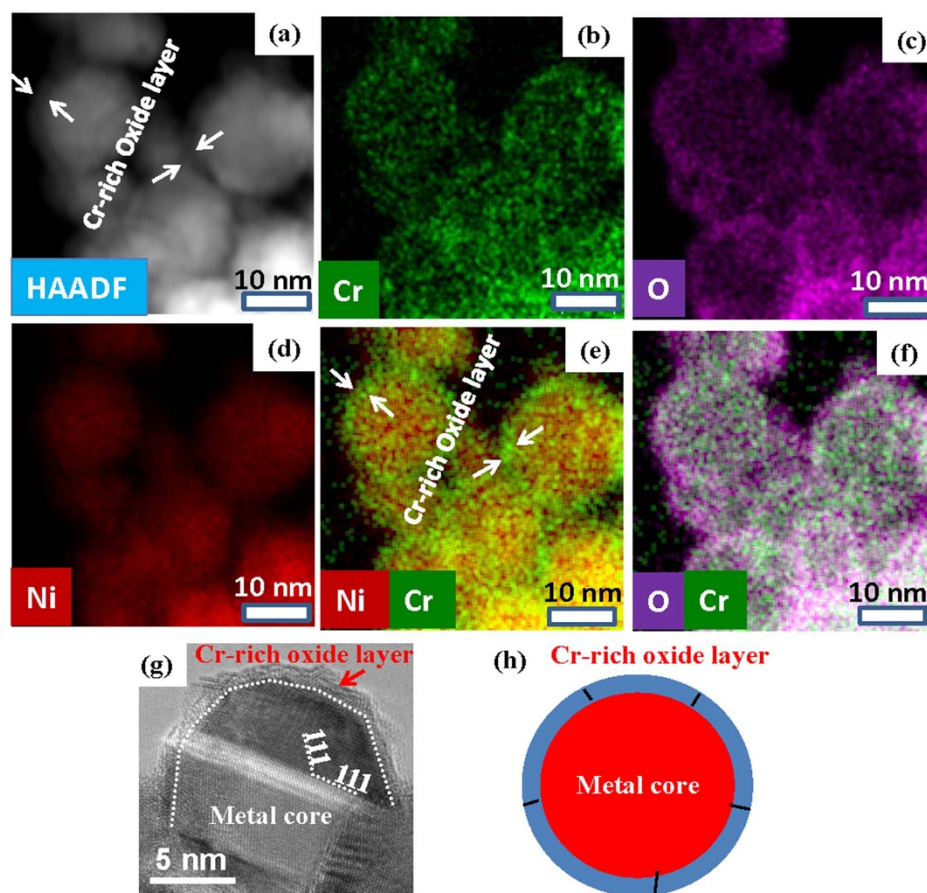


Figure 4 | STEM-HAADF image and EDS elemental maps showing the spatial distribution of Ni, O, and Cr in Ni5Cr nanoparticle, which was exposed to air at room temperature. (a) STEM-HAADF image revealing an oxide layer. (b) Cr map. (c) O map. (d) Ni map. (e) Ni + Cr map. (f) O + Cr map. (g) HRTEM image showing core-shell structure. (h) Schematic drawing of the core-shell morphology. The EDS mapping reveals that the surface oxide is rich of Cr and O.

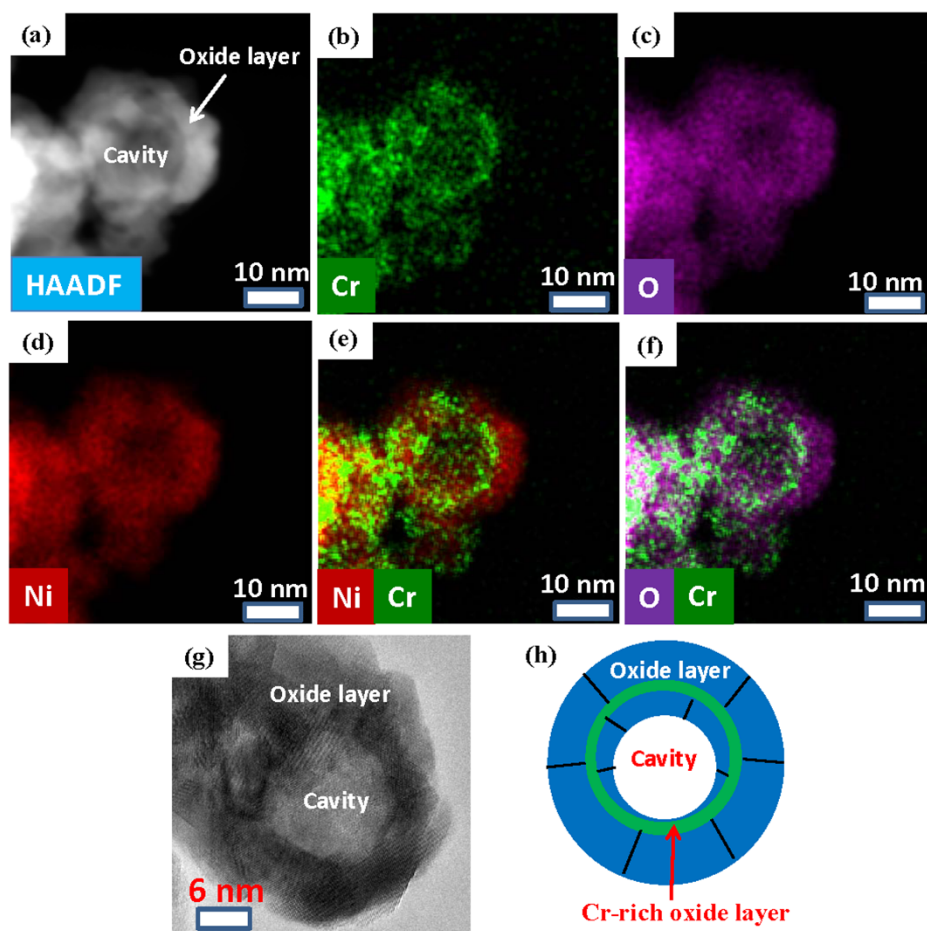


Figure 5 | STEM-HAADF image and EDS elemental maps showing the spatial distribution of Ni, O, and Cr in Ni₅Cr nanoparticle following the high temperature oxidation. (a) STEM-HAADF image revealing an hollow structured oxide particle. (b) Cr map. (c) O map. (d) Ni map. (e) Ni + Cr map. (f) O + Cr map. (g) HRTEM image showing hollow structure. (f) Schematic drawing of the hollow structure and the trapping of Cr-rich oxide layer. Comparing the dimension of the cavity and the Cr-rich oxide layer, it is obvious that the Cr-rich oxide layer is embedded in the nickel oxide.

anion to cation diffusion. The addition of Cr at 5 at% to Ni increases the rate of vacancy injection as compared with pure Ni. More work is needed to systematically vary the alloy composition to determine how various alloy additions alter vacancy injection.

We conclude that direct in-situ TEM imaging and high sensitive EDS elemental mapping reveal unprecedented structural and chemical information of Ni and Ni₅Cr nanoparticle during high temperature oxidation. The oxidation is featured by multi-site oxide nucleation, followed by the formation of an oxide layer through growth and impingement of the oxides. Supersaturation of injected vacancies leads to the nucleation of a single cavity at the interface between the oxide and the metal, which acts as an effective sink for absorbing the vacancies injected during the subsequent oxidation. Formation of cavity leads to an accelerated oxidation. For the case of Ni₅Cr alloy, the Cr is preferentially oxidized even during the initial oxidation at room temperature, indicating a high mobility of Cr in the Ni lattice. Due to the selective oxidation of Cr, the oxidized nanoparticle shows unique chemical distribution with Cr rich oxide embedded into the NiO. More generally, the nanoscale selective oxidation can be used to tailor new materials with a spatially controlled chemical distribution and functionality.

Methods

Both pure Ni and Cr-doped Ni nanoparticles were synthesized using the cluster deposition method described in detail previously^{25,26}. Cr dopant concentration is 5 at%. For convenience, the pure Ni and Ni doped with 5 at% Cr samples were correspondingly designated as Ni and Ni₅Cr, respectively. The deposition process was completed in a nanocluster deposition system, which combines a new kind of

sputtering-gas-aggregation cluster beam source with an atom beam from magnetron sputtering. The dopant concentration is controlled by adjusting the relative sputtering area of Ni and Cr on the target. The size of the nanoparticles depend on the He:Ar ratio, pressure inside the aggregation chamber and the growth distance the clusters

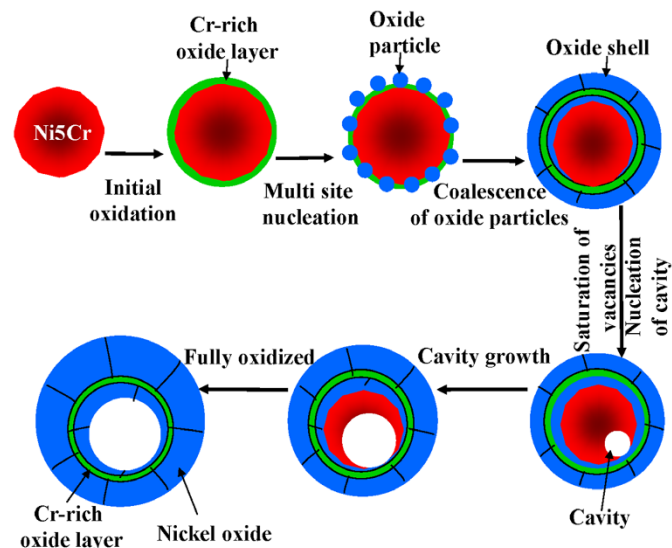


Figure 6 | Schematic drawing illustrates the structural and chemical evolution of the Ni₅Cr alloy particle during the initial room temperature oxidation and followed by high temperature oxidation.



travel inside the aggregation chamber. The deposition rate was variable up to 10 mg/h, measured in situ with a rotatable quartz microbalance. The morphology of the particles depends on the material and the average particle size. The general structural features of Fe particles synthesized by this method have been reported in detail in previous publications^{10,14,27}. Particles were initially deposited in a deposition chamber. After deposition they were exposed to ambient air, leading to the initial oxidation of the nanoparticle and formation of a thin oxide layer on each nanoparticle. The structural feature of this oxide layer has been studied in detail and previously reported²¹.

The oxidation behavior and structural evolution of Ni and Ni₅Cr were carried out by two methods. In the first method, the nanoparticles were loaded on the frame of Au TEM grid. The oxidation was carried out using a tube furnace in air at 200°C and 300°C. For oxidation at 200°C, the oxidation time was stepwise increased and following each step of oxidation, the particle structure was analyzed by TEM imaging. The oxide layer thickness as a function of accumulated oxidation time was drawn. In the second method, the oxidation experiments were performed using a dedicated field-emission environmental TEM (ETEM, FEI Titan 80–300). The ETEM is equipped with an objective-lens spherical aberration corrector and controlled gas pressure around the sample using a differential pumping system. To reduce the electron knock on damage effect on the sample, all the oxidation experiments for in-situ TEM were carried at 80 kV. The nanoparticle is loaded on an Au TEM mesh and heated to 375°C using a resistant coil heating holder (Gatan, USA). A gas mixture of 25% O₂ and 75% Ar with a total pressure of 1 mbar was established around the sample in the ETEM column. The structural evolution of the nanoparticle during oxidation is continuously recorded at a speed of 2 frames/s.

The elemental distribution in the Ni₅Cr particle before and after oxidation was mapped using energy dispersive x-ray spectroscopy (EDS). The EDS analysis was conducted using a Tecnai OsirisTM S/TEM microscope (FEI, USA) operated at 200 kV and equipped with an FEI Super-XTM detector system, which combines four symmetrically positioned Si drift detectors (SDD) around the objective lens with a high-brightness gun as detailed in a recent publication²⁸. This combination provides enhanced generation of X-rays, together with high detector efficiency, results in a faster mapping of larger areas in EDS spectrum images (SIs). The improvement in signal is roughly a factor of 50 leading to minutes of acquisition for mapping instead of hours previously. In this work, SIs are obtained by summing multiple frames where each frame is obtained with very short dwell times (typically on the order of tens of microseconds) per pixel. This helps to reduce specimen damage as the beam is not parked on any specimen region for a long period of time. Each 1024 × 1024 pixel SI was acquired with a total time of 14 minutes. The elemental distribution was also mapped using STEM-EELS, which was carried out on Titan 80–300 (FEI, USA) microscope fitted with a probe forming lens spherical aberration corrector and postcolumn attached with Gatan Image Filter (GIF) (Quantum 965). An energy dispersion of 0.25 eV/channel was used and the energy resolution of the system is ~0.8 eV.

1. Yang, J. C. & Zhou, G. In situ ultra-high vacuum transmission electron microscopy studies of the transient oxidation stage of Cu and Cu alloy thin films. *Micron* **43**, 1195–1210 (2012).
2. Zhou, G., Slaughter, W. S. & Yang, J. C. Terraced hollow hxdie pyramids. *Phys. Rev. Lett.* **94**, 246101 (2005).
3. Hou, P. Y. & Stringer, J. The effect of aluminum as an alloying addition or as an implant on the high-temperature oxidation of Ni-25Cr. *Oxidation of Metals* **34**, 299–321 (1990).
4. Fromm, E. Chapter 3 Low Temperature Oxidation, *Kinetics of Metal-Gas Interactions at Low Temperature: Hydriding, Oxidation, Poisoning*. 78–122 (Springer, 1998).
5. Railsback, J. G., Johnston-Peck, A. C., Wang, J. W. & Tracy, J. B. Size-dependent nanoscale Kirkendall effect during the oxidation of nickel nanoparticles. *ACS Nano* **4**, 1913–1920 (2010).
6. Cabrera, N. & Mott, N. F. Theory of the oxidation of metals. *Rep. Prog. Phys.* **12**, 163–184 (1948–1949).
7. Chenna, S., Banerjee, R. & Crozier, P. A. Atomic-scale observation of the Ni activation process for partial oxidation of methane using in situ environmental TEM. *Chem. Cat. Chem* **3**, 1051–1059 (2011).
8. Smigellkas, A. D. & Kirkendall, E. O. Zinc diffusion in alpha brass. *AIME* **171**, 130–142 (1947).
9. Yin, Y. *et al.* Formation of hollow nanocrystals through the nanoscale Kirkendall effect. *Science* **304**, 711–714 (2004).
10. Wang, C. M. *et al.* Void formation during early stages of passivation: initial oxidation of iron nanoparticles at room temperature. *J. Appl. Phys.* **98**, 094308 (2005).
11. Fan, H. J., Gosele, U. & Zacharias, M. Formation of nanotubes and hollow nanoparticles based on Kirkendall and diffusion processes: A Review. *Small* **3**, 1660–1671 (2007).

12. Nakamura, R., Lee, J. G., Mori, H. & Nakajima, H. Oxidation behaviour of Ni nanoparticles and formation process of hollow NiO. *Philos. Mag.* **88**, 257–264 (2008).
13. Fan, H. J. *et al.* Influence of surface diffusion on the formation of hollow nanostructures induced by the Kirkendall effect: The basic concept. *Nano Lett.* **7**, 993–997 (2007).
14. Wang, C. M. *et al.* Morphology and oxide shell structure of iron nanoparticles grown by sputter-gas-aggregation. *Nanotechnology* **18**, 255603 (2007).
15. Yin, Y. & Alivisatos, A. P. Colloidal nanocrystal synthesis and the organic-inorganic interface. *Nature* **437**, 664–670 (2005).
16. Svoboda, J., Fischer, F. D. & Vollath, D. Modeling of formation of binary-phase hollow nanospheres from metallic solid nanospheres. *Acta Mater.* **57**, 1912–1919 (2009).
17. Atkinson, H. V. A review of the role of short-circuit diffusion in the oxidation of nickel, chromium, and nickel-chromium alloys. *Oxidation of Metals* **24**, 177–197 (1985).
18. Schreiber, D. K., Olszta, M. J. & Brummer, S. Directly correlated transmission electron microscopy and atom probe tomography of grain boundary oxidation in a Ni-Al binary alloy exposed to high-temperature water. *Scripta Mater.* **69**, 509–512 (2013).
19. Chenna, S. & Crozier, P. A. In situ environmental transmission electron microscopy to determine transformation pathways in supported Ni nanoparticles. *Micron* **43**, 1188–1194 (2012).
20. Jinschek, J. R. Atomic scale structure-function relationship of heterogeneous catalysts: investigation of gassolid interactions by ETEM. *Microscopy and Analysis*, **2012**, 5–10 (2012).
21. Wang, C. M. *et al.* Microstructure of the native oxide layer on Ni and Cr-doped Ni nanoparticles. *J. Nanosci. Nanotech.* **11**, 8488–8497 (2011).
22. Zhou, G. *et al.* Step-Edge-Induced Oxide Growth During the Oxidation of Cu Surfaces. *Phys. Rev. Lett.* **109**, 235502 (2012).
23. Atkinson, A. Transport processes during the growth of oxide films at elevated temperature. *Rev. Mod. Phys.* **57**, 437–470 (1985).
24. Andreev, Y. Y. & Shumkin, A. A. A new theoretical approach to the thermodynamic calculation of high-temperature oxidation of Ni-Cr alloys. *Protect. Met.* **42**, 221–226 (2006).
25. Antony, J., Qiang, Y., Baer, D. R. & Wang, C. M. Synthesis and characterization of stable iron-iron oxide core-shell nanoclusters for environmental applications. *J. Nanosci. Nanotech.* **6**, 568–572 (2006).
26. Qiang, Y. *et al.* Iron/iron oxide core-shell nanoclusters for biomedical applications. *J. Nanoparticles Res.* **8**, 489–496 (2006).
27. Wang, C. M. *et al.* Morphology and electronic structure of the oxide shell on the surface of iron nanoparticles. *J. A. Chem. Soc.* **131**, 8824–8832 (2009).
28. Genc, A. *et al.* XEDS STEM tomography for 3D chemical characterization of nanoscale particles. *Ultramicroscopy* **131**, 24–32 (2013).

Acknowledgments

This work was supported by the US Department of Energy (DOE), Office of Basic Energy Sciences. The work was conducted in the William R. Wiley Environmental Molecular Sciences Laboratory (EMSL), a DOE User Facility operated by Battelle for the DOE Office of Biological and Environmental Research. Pacific Northwest National Laboratory is operated for the DOE under Contract DE-AC06-76RLO 1830. The nanoparticles used in this work were prepared by Professor Qian You of University of Idaho.

Author contributions

C.M.W., D.R.B. and S.M.B. designed the experiment, C.M.W. and A.G. carried out the in-situ TEM study. H.C. and L.P. carried out the EDS analysis. C.M.W. wrote the manuscript and all authors discussed the results and contributed to the writing of the manuscript.

Additional information

Supplementary information accompanies this paper at <http://www.nature.com/scientificreports>

Competing financial interests: The authors declare no competing financial interests.

How to cite this article: Wang, C.-M. *et al.* In-Situ TEM visualization of vacancy injection and chemical partition during oxidation of Ni-Cr nanoparticles. *Sci. Rep.* **4**, 3683; DOI:10.1038/srep03683 (2014).



This work is licensed under a Creative Commons Attribution-NonCommercial-NoDerivs 3.0 Unported license. To view a copy of this license, visit <http://creativecommons.org/licenses/by-nc-nd/3.0>